

The Handbook of Optical Coherence Tomography

B. Bouma and G. Tearney, eds., 421-443

Marcel Dekker, Inc. (2002)

**APPLICATIONS OF OPTICAL COHERENCE TOMOGRAPHY
TO THE STUDY OF POLYMER MATRIX COMPOSITES**

Joy P. Dunkers

Polymer Composites Group

Polymers Division

National Institute of Standards and Technology

Gaithersburg, MD 20899

INTRODUCTION

The use of optical coherence tomography (OCT) to study polymer matrix composites (PMCs) is very recent. So recent, in fact, that the full potential and limitations of this technique have yet to be studied completely since PMCs are a large and varied class of materials. At the onset of this program, OCT was pursued as a technique to non-destructively study PMCs because it offered a combination of spatial resolution and depth of penetration that was not currently available. Research efforts have been focused thus far on fiberglass reinforced composites, although some work has been done on Kevlar[®].¹ A comparison of OCT and more traditional non-destructive evaluation (NDE) techniques in the area of PMCs is provided later in this chapter. The discussion will focus on OCT as an NDE tool for microstructural and defect characterization and damage assessment. Since this chapter is a departure from the rest of this book, an introduction to PMCs to provide background and direction is given below.

POLYMER MATRIX COMPOSITES (PMCs)

PMCs are heterogeneous materials consisting of, in general, a polymer matrix and reinforcing fibers. The fibers provide the load bearing capability and are generally classified as either inorganic, with glass being the largest category, or organic. Carbon fibers are the most common type of organic based reinforcement but polymeric fibers like Kevlar[®] are also widely utilized. Initially, the discussion will be focused on both carbon and glass. Then, the bulk of the discussion will shift towards the glass reinforcement because OCT cannot image carbon fiber reinforced composites. Carbon strongly absorbs visible and near infrared light. The selection of fibers influences the following properties of the PMC: specific gravity, tensile strength and modulus, compressive strength and modulus, fatigue strength, electrical and thermal conductivities, and cost. The reinforcement can exist as short fibers that range from several hundred micrometers long to many millimeters in length or as continuous fibers that are meters long. Continuous fibers can be woven into two or three dimensional fabrics, depending on the load bearing requirements. An example of an application that has load bearing requirements is the use of glass reinforced PMC in bridges for decks, reinforcing bars, tendons, cables, beams, columns, and paneling.² Figure 1 shows a bridge erected in Scotland with composite cables, towers, and deck.²

The polymer matrix aids in forming the fibers into a final structure, contributes toughness to the composite by transferring loads between fibers, and protects the fibers from chemical and physical degradation. The choice of matrix material depends upon the desired end-use properties such as adhesion to the fibers, modulus, shrinkage, thermal stability, corrosion resistance, and specific chemical resistance. The matrix for a composite can be thermoplastic or thermoset. A thermoplastic matrix is a fully reacted polymer of several thousand repeat units that can repeatedly be heated and reshaped. In contrast, a thermoset matrix begins as small molecules and reacts during fabrication to form a cross-linked network with virtually infinite molecular mass. This solid is permanent and cannot be re-shaped upon heating, but it more resistant to attack by organic fluid. Composites are usually designed so that fibers carry the loads, leaving the matrix to play a secondary role. The matrix provides resistance to buckling of fibers loaded in compression and transfers load between fibers and around fiber breaks when they are in tension. Even the best designs, however, cannot always avoid loads in directions not dominated by fibers. One example is delamination where loads perpendicular to the fiber layers cause the

layers to separate. For such cases, the properties of the matrix are very important. More basic information about polymer science and technology is available elsewhere.³ In this chapter, the composites of interest consist of a thermoset matrix and continuous glass fibers.

The fiber-matrix interface region, frequently called the interphase, is also important to composite performance. This region contains interactions, both chemical and physical, between the fibers and the matrix. The quality of the interphase has a substantial effect on the lifetime of the PMC. A good interphase, or interaction, is desired and will efficiently transfer load between fibers and support loads transverse to the fibers. A poor interphase may result in premature failure of the composite. Surface treatment of the fibers promotes adhesion between the fibers and matrix by depositing or generating molecules at the fiber surface.⁴ These molecules wet and may even react with the fiber surface at the same time they become entangled with or react with the matrix.

There are several reasons why polymer matrix composites are used over more traditional materials such as metal and wood. The biggest advantages are their high strength-to-mass and modulus-to-mass ratios and design flexibility. Other advantages are longer lifetime, mechanical damping, and controllable thermal and electrical conductivity. The biggest disadvantages include the high cost of raw materials and manufacturing, low toughness, environmental degradation, and the lack of standards for testing and long term performance. Although recycling is an issue in certain applications, the use of recycled PMC as filler in new parts is being implemented.⁵ Probably the biggest hurdle that inhibits the breakthrough of composites into high volume, commercial markets is bringing down the high cost of the composite by reducing waste through improving manufacturing methods and quality control. OCT can aid in this endeavor.

Traditionally, PMC were used in high cost applications such as commercial and military aircraft and weapons where decreasing weight is of greater concern than cost. Some specific PMC components that have been used are wings, rotors, tails, rudders, fins, and ailerons.⁶ In a recent application, a business jet fuselage was built with a carbon fiber honeycomb composite that was made in only two pieces. This PMC fuselage weighs less than 1000 lbs. and provides more cabin space because of reduced wall thickness when compared to aluminum.⁷ PMCs are not simply limited to high performance, high cost aircraft and aerospace applications. They have expanded into the transportation, marine, infrastructure, construction, and consumer markets.

For example, the body panels of the Chevrolet Corvette are made out of glass reinforced composites.⁸ In 1996, a nylon-6,6 and glass fiber air intake manifold was introduced on the Ford Mustang V8.⁹ Now, all General Motors air intake manifolds and fuel injector rails are glass reinforced nylon-6,6. Spoolable composite pipe and tubing products constructed with thermoplastic liners for corrosion resistance and pressure containment are being installed into North Sea oil wells.¹⁰ In addition to power and sail boats, PMC have also been used in sea walls, pilings, and docks. In the construction industry, decking, roofing, and walkways have been made with PMC. Bridge columns in California have been wrapped with carbon fiber embedded in epoxy to provide additional support against earthquakes.¹¹ The first composite reinforced concrete deck on a vehicular bridge was built over Buffalo Creek in McKinleyville, West Virginia.¹² The incorporation of composites in the consumer industry is found mainly in sporting goods and are best known in golf club shafts and fishing rods. Tennis rackets made with carbon fiber composites have the rigidity required to produce a more accurate shot than traditional wood rackets. Stiff composite frames on bicycles prevent twisting on rugged terrain

while still affording weight savings, and carbon fiber skis and ski poles are also entering the market.¹³

With all of the aforementioned examples of applications of PMCs, why the interest in the non-destructive evaluation of these materials? Although composites have demonstrated superior performance in many applications, their high cost prevents them from gaining in-roads into high volume, cost competitive markets. The major obstacle in cutting the cost of PMC lies in increasing the speed of the manufacturing process while maintaining or increasing the quality of the resulting composite part. This is where NDE plays a role in cutting costs.

The final properties of a composite are highly dependent upon, among other variables, microstructure and defects. Microstructure is defined as any physical characteristic within the PMC that can be identified with some regularity. Defects are physical characteristics that are not planned and prevent the composite from achieving optimal properties. For example, the size and shape of glass tows are considered microstructural characteristics. How the layers of glass orient themselves when the mold is closed is also considered microstructure. Any microscopic or macroscopic void in the reinforcement is considered a defect. Wrinkling of the reinforcement in the final part is considered a defect. Microstructure and defects are highly influenced by the manufacturing or processing of the PMC. For example, in fabrication by resin transfer molding where the reinforcing fibers are placed in a mold and the matrix resin is then injected, the number, size, and mechanism of voids formed were found to be dependent upon the reinforcement type and injection pressure.¹⁴ The effects of voids upon shear, tensile, and flexural strengths have been the subject of much study.^{15,16,17} The final composite properties are heavily, although not solely, dictated by the microstructure and defects. The need for a microstructure and defect characterization tool led to the exploration of OCT of composites.

NON-DESTRUCTIVE EVALUATION OF PMCs

OCT has some advantages and disadvantages over conventional NDE techniques. This discussion of NDE is limited to those techniques that are mainstream or similar to OCT. An analogous optical technique used widely in the biological community is confocal optical microscopy. There is very limited information in the literature about confocal optical microscopy of PMCs.¹⁸ The most likely explanation for this is that the highly scattering nature of composites makes any appreciable depth of field impossible with confocal microscopy. It has already been demonstrated that the resolution, depth of field, and dynamic range of OCT are far superior to confocal optical microscopy for PMCs.¹⁹

Ultrasonic imaging is a good method to compare with OCT because ultrasound is a major NDE technique. Both transducer and laser based ultrasonics have been used on composites, although measurements with a transducer are complicated by the requirement of a coupling material between the transducer and composite. The practical resolution of ultrasonics is on the order of hundreds of micrometers with tens of millimeters penetration depth.^{20,21} Ultrasound imaging is primarily used to observe defects and works best with planar samples.²⁰ A major drawback to ultrasonics is that the depth of a feature must be determined by model studies, whereas, it is known precisely using OCT. Both OCT and ultrasonics suffer from contrast degradation and shadowing through the sample thickness. However, ultrasound can successfully image voids and damage in carbon fiber reinforced composites whereas OCT cannot.

X-ray based techniques are used extensively to evaluate damage and have been applied less frequently to the examination of voiding and tow placement. Composite damage has been studied with x-ray radiography.^{22,23} All x-ray techniques rely on the contrast generated by the differences in the attenuation of the x-ray beam to differentiate heterogeneity from undisturbed material. Unlike ultrasound, this technique is non-contact. However, it may be necessary to use a dye tracer to provide contrast between the damage zones and the rest of the composite. Also, superposition of features can confound interpretation with this conventional film radiography. A more recent technique, x-ray computed tomography (CT), relies on the measurement of transmitted radiation from many angles to reconstruct an image of the composite.²⁴ X-ray CT can be used to detect various heterogeneities such as resin/fiber distribution, anisotropic fiber structure, voiding and porosity, as well as damage events. The x-ray transmission is limited by the density, size and atomic number of material and x-ray source available. Perhaps the biggest drawback is the spatial resolution, which is typically 500 μm . With specialized sources and detectors, the spatial resolution can approach a few tens of micrometers with objects tens of millimeters in maximum dimensions at great cost.²⁴

Nuclear magnetic resonance (NMR) imaging has been performed on composites with some success,²⁵ but has one major drawback. Imaging of glassy polymers such as epoxy is very difficult because of the very long spin-lattice relaxation time (T_1) that leads to line broadening and a very short spin-spin relaxation time (T_2) that cannot be detected with current electronics. Thus, samples are usually imbedded with a liquid, and it is the relaxations of the liquid that are monitored. The spatial resolution is comparable to OCT, reportedly down to 10 μm .²⁶ In addition, carbon fiber composites can be imaged in the majority of cases, except where the plane of the laminate sheets is perpendicular to the radio-frequency (RF) field since the conductive sheets screen the RF field within the coil.²⁷ But as with ultrasound, voids and other defects are usually imaged instead of microstructure.

OCT INSTRUMENTATION

The imaging system used for the experimental work described in this chapter is from the laboratory of Professor James Fujimoto at the Massachusetts Institute of Technology, Cambridge, MA and is shown schematically in Figure 2.²⁸ A commercial superluminescent light source was used. The source operated at 1.3 μm with an output power of up to 15 mW and a spectral bandwidth of 40 nm, corresponding to an axial spatial resolution of ≈ 20 μm . The laser light was coupled into a single-mode fiber-optic Michelson interferometer and delivered to both the reference mirror and the sample. The reference mirror was mounted on a rotating galvanometer, which was driven with a sawtooth voltage waveform. Transverse scanning was performed using a computer controlled motorized stage to translate the sample.

The interferometric signal was electronically filtered with a bandpass centered on the fringe or heterodyne frequency. The filtered fringe waveform was then demodulated, digitized and stored on a computer. The high dynamic range of this system allowed back-reflections as low as femtowatts to be detected. Images were displayed by mapping the logarithm of the signal strength to a gray scale look-up table. The acquisition time for each image was approximately 1 min. The axial (z) measurement range was determined by the distance moved by the reference mirror (4.5 mm) normalized by the refractive index (n) of the sample: 4.5 mm/ n . For the epoxy matrix samples discussed here, the refractive index was 1.55. For the vinyl ester matrix sample, the refractive index was 1.55 for the low void sample and 1.46 for the high void sample. The

probe beam was focused to a 30 μm diameter spot at a depth of approximately 750 μm to 1000 μm below the surface of the sample. For the images presented here, (1.5 to 2) mm depth can be resolved with good contrast. More recent work indicates that at least 4 mm can be resolved in these samples.

The OCT images were taken for both the epoxy and vinyl ester matrix composites with the fibers oriented perpendicular to the laser as shown in Figure 3.²⁹ For any position along the x axis, reflections that represent heterogeneities are collected as a function of z. The sample is then moved with a motorized stage to image a new x,z slice of the composite, and this process is repeated for various positions along the fiber, or y axis. The transverse resolution along the x axis is estimated to be 40 μm . The transverse resolution is governed by spot size and scan rate: there is an inverse relationship between transverse resolution and sampling depth. The axial resolution along the z axis is 20 μm . The images typically contained (300 or 350) x 450 pixels. All samples were tilted 4° to avoid collection of the laser reflection from the top surface.

OPTICAL COHERENCE TOMOGRAPHY OF POLYMER MATRIX COMPOSITES

Imaging of Microstructure and Defects

The following discussion focuses on some of the very first results we obtained on PMC.²⁹ The composite samples of initial interest for OCT were composed of 7 layers of a unidirectional E-glass fabric in an epoxy resin. Figure 4 shows an OCT image of the entire cross-section of the composite. The image is 6.0 mm wide (x axis) and 3.7 mm deep (z axis). Each tow is typically 1 mm wide and 550 μm thick. A tow is a bundle of the individual glass filaments. This image is a composite of two images taken from the top and bottom of the sample at the same y position as shown in Figure 3. The bottom image quality is slightly degraded compared to the top image due to the difference in quality between the top and bottom surfaces. The dark ellipses indicated by an arrow are the polyester threads that are stitched to hold each layer of the fabric together. The light regions outside of the tows are identified as resin rich areas, and the medium gray regions are the fiber tows. The black spots within the fiber tows could be voids from incomplete wetting of the fiber tows and consequent air entrapment. However, care must be taken when interpreting these images for the following reasons.

It is well known that the contrast between features degrades as a function of depth because of scattering of photons. This contrast degradation is much more pronounced than for biological materials. For this particular figure, since it is a composite of top and bottom images, the noise increases as you move towards the center of the sample thickness. The intensity of the light reaching a particular depth for any position across the sample is affected by how strongly features directly above that position reflect or randomly scatter the light. Although the structure of this sample is somewhat regular, it is difficult to predict its effects on the scattered light. Therefore, for any particular depth within the sample, the intensity of a pixel or group of pixels cannot be assigned to a particular feature upon first inspection. For example, a light area within a tow could result from a resin rich region, the destructive interference caused by a group of fibers, or shadowing from a strongly reflecting feature from above. In addition to lens and interference effects in the sample, another source of noise arises from the gray vertical lines that project from the black reflection at the air/composite interface. These lines are a result of detector saturation from the signal at that strongly reflecting interface. In fact, the noise from the instrumentation is far below the level of noise generated from the sample itself. From the above discussion, it is obvious that the best way to differentiate real features from artifacts is to

evaluate a number of slices from a different perspective, perhaps along the x-y plane at a particular z position.

The OCT volumetric image of the epoxy/unidirectional E-glass composite has been reconstructed, as shown in Figure 5 so that it may be re-sliced along any plane of interest for inspection.²⁸ The image dimensions are 6.00 mm along the x axis, 1.48 mm along the z axis, and 3.85 mm along the y axis. The gray ellipses are the fiber tows which are approximately 2 mm wide and 750 μm thick and consist of about two thousand, (10 to 20) μm diameter glass fibers.³⁰ The long axis of the tows is shown on the x-y plane. The polyester stitching that holds a single layer of tows together is indicated by the black arrows. Upon closer inspection, small dark areas are evident inside the fiber tows. These dark areas are high reflectivity regions indicative of individual voids. During the molding process, air can become entrapped as channels in tows if there is insufficient driving pressure, high resin viscosity or low reinforcement permeability.³¹ Also, OCT images provide important information about the permeability of the reinforcement since the stacking of the layers has a large influence on the infiltration of the resin with the reinforcement, as we will see later. A preform with the tows in a nested configuration has about a 50 % lower permeability than the same material with the tows in a stacked configuration.^{32,33}

Figure 6 displays a cross-section of the composite along the x-y plane at 740 μm from the top which bisects the middle row of tows in Figure 5.³⁴ The dark features of high reflectivity shown by arrow 1 are the polyester threads that holds the layer of tows together. The dark, elongated regions parallel to the y axis are thought to be voids (arrow 2). However, the issue of contrast degradation through the thickness can be assessed with a simple calculation. Power reflectivity for the fiber/resin and resin/void interface can be easily calculated: $[(n_1-n_2)/(n_1+n_2)]^2$. This equation suggests that the voids will be much higher back-reflecting than the fibers. Therefore, as we lose signal because of scattering attenuation, one should clearly see the voids much deeper inside the sample than the fibers. There are also geometric effects on the reflectivity which depend on the shape of the reflecting/scattering boundary and can be included in the modeling. Roughly speaking, the back-reflected signal will also be larger if the boundary has less curvature. With known reflectivity and scattering, one could estimate features (i.e. voids) at different positions along the z axis. The correlation between voids and depth of penetration is demonstrated further in the following figures.

Figure 7 contrasts the OCT cross-sectional images of the low (a) and high (b) void content vinyl ester resin and glass samples as discussed in previous work.²⁹ These images are uncorrected in the axial direction. In Figure 7a, individual fibers can be discerned near the top of the image. These fibers appear as a speckled pattern. As discussed before, the contrast fades as a function of depth in the images, so fewer of the individual fibers can be discerned. In Figure 7b, some individual fibers can be identified. More importantly, there are larger black features that can be correlated with the existence of voids, as shown in the next figure.

Figure 8a is the re-scaled Figure 7b and compares the OCT image of the high void content composite with the corresponding optical micrograph, 8b. The OCT image was collected at 260 μm in the z direction while the optical micrograph was from a section taken at 270 μm . From multiple optical micrographs, these voids extend from at least (180 to 360) μm , making the comparison valid. The dimensions of Figure 8a are 5.1 mm wide and 1.9 mm deep, and the dimensions of Figure 8b are 5.1 mm wide and 1.8 mm deep. The dotted lines show the correspondence of representative voids in the OCT and the optical microscopy images. The

voids observed in the micrograph image, 8b, can be seen in the OCT image, 8a, but the delineation of the void boundaries are not as pronounced in the latter. The small, resin rich areas in Figure 8b are not detected in the OCT image.

Figure 9a displays an OCT image of the low void sample and the corresponding optical micrograph in Figure 9b. The dimensions of Figure 9a are 6.0 mm wide and 2.0 mm deep. Although some correspondence can be made at shallow penetration depths, it is difficult to identify the resin rich areas in 9a that are so prominent in the 9b. The dimensions of Figure 9b are 6.2 mm wide and 1.7 mm deep. Figure 9b is 170 μm along the z axis. Multiple OCT images are essentially identical from 180 μm to 2180 μm along the z axis. The OCT image is featureless for two reasons. The first is the previously mentioned attenuation as a function of depth. The second is the fact that small features that do not have large refractive index differences, like embedded voids, are difficult to detect since boundaries can become blurred in this technique.

Other types of reinforcement were also imaged in previous work.²⁸ The volumetric reconstruction of the epoxy/0-90° woven composite is shown in Figure 10. In this image, tows that run along the x axis are positioned above and below tows that are parallel to the y axis. The image dimensions are 6.14 mm along the x axis, 2.13 mm along the z axis, and 4.95 mm along the y axis. Arrow 1 identifies the tows along the x axis that are crossing over the tows along the y axis. Arrow 2 shows the tows along the y axis that are crossing over the tows along the x axis. The layer microstructure has a direct influence on mechanical properties and has been studied elsewhere³⁵. Now that we have established that OCT can be used to examine composite microstructure, we present an example of how the microstructure, obtained using OCT, influences real properties.

An important fiber reinforcement property for manufacturing is the permeability. Permeability is the factor that controls the rate of fluid flow through the mold during the manufacturing of the PMC. Knowledge of the permeability tensor in liquid composite molding is important for process optimization. Unfortunately, experimental determination of the permeability is difficult and time consuming.³⁶ In previous work, binary images were generated from the OCT data and input into a lattice-Boltzmann fluid flow model for permeability prediction.³⁷ Calculated permeabilities were compared to experimental values for the same fiber volume fraction.

Fluid flow in Liquid Composite Molding (LCM) processes such as resin transfer molding (RTM) is usually modeled using Darcy's Law given by

$$\mathbf{v} = -\frac{\mathbf{K}}{\mu} \cdot \nabla P \quad (1)$$

where \mathbf{v} is the vector of average (superficial) velocity in the medium, P is the pressure, \mathbf{K} is the symmetric, second order permeability tensor, and μ is the fluid viscosity. Darcy's law is a volume-averaged model in which all the complicated geometry of the fiber preform structure is accounted for through the permeability. Accurate permeability data, therefore, are a critical requirement if *a priori* modeling efforts based on Darcy's law are to be successfully used in the design and optimization of these processes. Currently, the most reliable and commonly used technique for obtaining permeability values is experimental measurements in either radial or uni-directional flow configurations.³⁸ However, experimental characterization is slow, as it involves

a large number of carefully controlled experiments over a large range of volume fractions. Another more serious limitation is the difficulty conducting experiments on the materials in the deformed states they encounter when placed in LCM tooling, although there have been some recent efforts.³⁹

In light of these limitations, computational prediction of permeability^{33,40,41,42} offers a potentially accurate and robust alternative to experimental methods. Such calculations involve imposing a pressure drop across the media, solving the appropriate transport equations for the detailed flow field, and then back-calculating the permeability by applying Darcy's law. The biggest drawback of this approach has been the inability to determine quickly and accurately the detailed geometry of the fibrous preform materials, which in addition to many intricate structural features, typically contain statistical variations and defects in their microstructure.⁴³ Without a precise representation of the media, it is not possible to accurately predict permeability values using computational methods.

There have been two main approaches to the problem of microstructure determination. The first is to perform calculations on small, computationally efficient "unit cell" structures using nominal dimensions that represent the average preform structure. The major problem with this approach is that calculations on the "average" unit cell structure do not in general, yield an accurate value for the average permeability.⁴³ A second approach is to determine the microstructure via optical methods (e.g., microscopy), and directly perform the numerical calculation on a discretization of the optical image. This approach has the advantage of exactly representing the media, and by including large sections of the media in the image, variations and defects in the microstructure are automatically accounted for in the calculation. However, until recently, this approach was probably even more tedious to perform than direct experimental measurement of permeability since the composite specimens typically had to be carefully sectioned, polished and examined. However, OCT offers a means for rapidly and non-destructively determining the microstructure of fiber reinforced plastic materials.

Governing Equations

Modeling the flow in fibrous reinforcement is complicated by the existence of an open region outside of the tows and micro-pores created by the individual fibers inside the tows. Following previous studies,^{33,40,41,42,43} the Stokes equation, given by

$$\nabla P = \mu \nabla^2 v \quad (2)$$

is used to model flow in the open regions. The Brinkman equation, given by

$$\nabla \langle P \rangle = \mu \nabla^2 \langle v \rangle - \mu \underline{\underline{K}}^{-1} \cdot \langle v \rangle \quad (3)$$

is used to model flow in the micro-pores created by the individual fibers inside the tows, where $\underline{\underline{K}}$ is the permeability of the porous tows. In both regions, the continuity equation,

$$\nabla \cdot v = 0 \quad (4)$$

is used to enforce conservation of mass.

Permeability Computation

Permeability for different flow directions was computed by imposing a constant pressure along opposite faces of the lattice in the desired direction and integrating the system of equations above to steady-state. Estimates for the intra-tow permeability values were obtained from the formulas given in previous work.³³ The steady-state velocity field at the inlet was integrated over the surface to obtain the flow rate, Q , and this was used in the formula

$$K_{eff} = \frac{\mu QL}{A\Delta P} \quad (5)$$

to obtain the effective permeability, K_{eff} , for the desired direction.

Before permeability could be predicted, the OCT images were converted to binary images in the following manner. An automated image processing program was written using MATLAB 5.1 with the Image Processing Toolbox to convert the raw gray scale OCT images to binary images of glass fiber and epoxy (Figure 11). The raw image is first rotated and cropped to eliminate sample tilt and edge effects. An example of this pre-processed image is provided in Figure 11a, where the darker ellipses correspond to the three cross-sectional layers of fiber tows while the lighter regions are due to the epoxy. The image is then doubled in size by linear interpolation of adjacent pixels to minimize any artificial alteration of the tow size in subsequent image processing. To increase the contrast between the darker tows and the lighter epoxy regions, a variance image is created by replacing the intensity value of a 2x2 cluster of pixels with the standard deviation of that cluster. In the next two steps, spurious light pixels within the tow regions and vertical lines corresponding to detector saturation are eliminated. Using the automated program, the boundary of the tows are determined and a binary image (Figure 11B) is formed. Smoothing and filling operations that maintain the area of the tows are being pursued. The resulting binary image is then used as input for the permeability modeling.

The results from the permeability calculation are shown in the table. The value for the experimental axial permeability (K) is $5.3 \times 10^{-4} \text{ mm}^2$ and results from one axial flow experiment. The axial K is the K measured along the fiber tows, or in the y direction as in Figure 5. The standard deviation (\pm) associated with it is taken from previous work with this reinforcement at higher fiber volume fractions.⁴⁴ Image sets for computing K values within this table were processed in two different ways: For the “Manual” method, the tow outlines were drawn by sight and filled in to generate a binary image. Images using the “Automated” method were processed as described in the previous paragraph. For Data 2, the axial K of $3.81 \times 10^{-4} \text{ mm}^2$ is considered to be the best possible value because the images are manually drawn. Part of the discrepancy between the experimental value for K and the calculated values may also originate from micro-scale variations of permeability within the fabric. The twenty one images used in these calculations represent only a width of 6.0 mm, a depth of approximately 1.5 mm, and, most importantly, a length of 1.0 mm. For comparison, the size of the reinforcement used in experimental determination of permeability is 15 cm wide, 1.3 cm deep and 15 cm long. The effect of micro-scale variation in the permeability can also be illustrated by comparing K from Data 1 and Data 2. The K from Data 1 is $4.45 \times 10^{-4} \text{ mm}^2$ and is calculated using five images, whereas the K from Data 2 is $3.81 \times 10^{-4} \text{ mm}^2$ and is calculated using twenty-one images. Data 5 is calculated on a totally different section of the composite and yields an axial permeability within the experimental error.

For the automatically processed images in Data 3, the axial K of $2.83 \times 10^{-4} \text{ mm}^2$ is much lower than for Data 2. For Table 1, the Brinkman fraction is defined as the area occupied by the tows. The higher the area occupied by the tows (or the higher the Brinkman fraction), the lower the K because there is less open space available for fluid flow. If the Brinkman fractions are considered, then the axial K for Data 3 should be higher than for Data 2 since the Brinkman fraction for Data 3 is slightly lower than for Data 2. From these results and from analysis of the fluid velocity data, we conclude that the roughness of the tow boundaries has a large influence on the velocity of the flow because it acts to increase the resistance to flow. This influence propagates to the middle of the channels between the tows where fluid velocity should be at a maximum.

This conclusion is supported by results from Data 6 when compared to Data 7. The images from Data 6 are originally from Data 2, the manually processed images. However, a small amount of roughness was introduced in Data 6 while retaining nominally the same Brinkman fraction. For Data 7, the images in Data 2 were dilated to increase the Brinkman fraction, but the roughness was not altered. When the axial K from Data 7 is compared to Data 6, the result is initially unexpected. A relative increase of roughly 4% of the Brinkman fraction in Data 7 should lead to a decrease in axial K over Data 6, but the result is the opposite. The axial K of Data 7 is higher than Data 6. This comparison between the permeabilities from Data 6 and Data 7 mean that an increase in roughness will have more of an impact on permeability than a similar increase in Brinkman fraction. These results also highlight the importance of processing the images as close to the actual structure as possible.

Imaging of Damage

Both microstructure and damage in polymer matrix composites are often characterized using destructive techniques such as microscopy on sectioned samples which provides detailed information on a small size scale. The capability to measure these features non-destructively, however, is very desirable since that permits monitoring of damage evolution and correlation of the results with microstructural features that can initiate, influence, or even control the damage. It is even more advantageous if these measurements are performed with a single technique because this eliminates the complications involved in combining data from different sources.

OCT has also been used for non-destructive evaluation of damage in composites in previous work.²⁸ This approach is important in providing an understanding of the initiation of failure since there is little in the literature about the NDE of damage initiation in composites. To illustrate the capability of OCT for imaging damage, an epoxy/uni-directional E-glass composite was subjected to impact damage, and imaging was performed along a surface crack. Figures 12A through 16A show the damage along the x-y plane through the first layer of composite and are all 5.50 mm wide and 1.98 mm high. Of course, there is always an issue of shadowing of highly reflecting features such as cracks. The resulting shadowing is not a consistent problem and requires further study. Figures 12B through 16B are y-z images showing the position of the tows designated by the dark colored crossing thread and are 1.98 mm wide (y axis) and 2.23 mm high (z axis). The arrow on the left of these figures indicates the position of the image in figures 12A through 15A with respect to the tow placement.

The damage at the surface of the composite is shown in figure 12A by the arrow, which points to the ridge created by the impact. Figure 13A shows a slice of the composite $337 \mu\text{m}$ below the surface. The black lines are drawn into this and subsequent figures to indicate the path of the

tows. Arrows 1 and 2 indicate cracks propagating through the fiber tow. Arrow 3 shows the polyester crossing threads that hold the top layer together. Figure 14A shows images that are 460 μm from the surface. The crack indicated by arrow 1 is beginning to propagate along the tow and resin boundary. It is about 820 μm long and is shown to be approaching the bottom of the tow in Figure 14B. The crack extends to 1.8 mm long in Figure 15A and is 550 μm from the surface as shown by arrow 1. The polyester stitching is still evident (arrow 2). Finally, a delamination zone is shown by the white arrow in Figure 16A at the interface between the bottom of the first tow layer and resin (Figure 16B). The delamination is about 1.9 mm wide and 0.50 mm high and 652 μm from the surface. This crack continues to propagate into the second layer, and a delamination area is found at 1.66 mm down as well. Damage in the direction of the tows is consistent with impact damage observed in other composites.⁴⁵ Comparison of these results with complementary techniques such as x-ray CT and optical microscopy is the subject of ongoing work.

SUMMARY AND FUTURE DIRECTIONS

This work has demonstrated the potential of OCT as a NDE tool for polymer matrix composites. OCT goes beyond typical composite NDE because of its ability to image microstructure in addition to damage, and has been shown to yield results in good agreement with optical microscopy. For the first time, microstructural information obtained non-destructively was used in the prediction of an important reinforcement property, the permeability. A more complex reinforcement was imaged showing the effect of mold compaction on layer placement and orientation, which is also important for permeability considerations. Of equal importance, OCT was used as a rapid non-destructive probe for damage, suggesting the concurrent use of mechanical testing and OCT. OCT provided absolute information on the location and size of the defects with the resolution required to detect damage initiation.

In the immediate future, in-house instrumentation will be used to optimize image collection by varying the confocal parameter, scanning and stage velocity, and bandpass. The potential applications of OCT to the field of PMCs are plentiful. Extending the permeability prediction to OCT images with more complex reinforcement is of great interest. Using OCT coupled with fatigue testing to monitor the initiation and progression of damage is also planned. Imaging of short fiber glass thermoplastic composites is extremely important for determination of fiber orientation distribution, a critical property of this material in a high volume market. However, short fiber glass in thermoplastic composites is nominally 10 μm in diameter and challenges the instrumental resolution. More far reaching ideas are using tunable sources to probe how moisture or other environmental fluids diffuse into the composite. Also, polarized OCT could be used to probe residual stress in composites which could help in understanding their design and failure.

ACKNOWLEDGEMENTS

I would like to gratefully acknowledge Professor James Fujimoto for the use of his OCT instrumentation and insightful discussions. There were a number of members of his laboratory that kindly shared their time and expertise with us including Drs. Brett Bouma, Jergen Herrmann and Xingde Li, and Mr. Rohit Prasankumar.

I also would like to thank the people in my group that contributed so much to the success of my work. I would first like to thank my group leader, Dr. Richard Parnas, for his full support of my work. I am grateful to Dr. Carl Zimba for much of the data collection and for his willingness to mentor me through a lot of explanation of the phenomena and hardware. There are also many other people that have contributed in their own way such as Drs. Frederick Phelan for the modeling, Donald Hunston for his help on the damage aspects of the work, and Richard Peterson for permeability measurements. I also wanted to specially acknowledge our technician, Ms. Kathleen Flynn, for doing all of the hard work.

Lastly, I also wanted to acknowledge Dr. Matt Everett and his group in the Medical Technology Program at Livermore National Laboratory for their continued efforts in helping me build an OCT system.

FIGURE CAPTIONS

Figure 1: Composite cables, decks, and towers at the Aberfeldy Bridge, Scotland.

Figure 2: Schematic representation of the solid state laser and OCT system layout.

Figure 3: Schematic showing the laser orientation and sampling directions with respect to the composite.

Figure 4: As collected OCT image of unidirectional E-glass fibers in epoxy resin.

Figure 5: OCT volumetric reconstruction of an epoxy/unidirectional E-glass composite.

Figure 6: An x-y cross-section that is 740 μm from the surface. Arrows indicate regions of high reflectivity that correspond to polyester stitching (1) and voids (2).

Figure 7: Images of vinyl ester resin/E-glass composites with low (A.) and high (B.) void content.

Figure 8: Comparison of OCT image (A.) and optical micrograph (B.) for high void vinyl ester resin/E-glass sample.

Figure 9: Comparison of OCT image (A.) and optical micrograph (B.) for high void vinyl ester resin/E-glass sample.

Figure 10: OCT volumetric reconstruction of an epoxy/0-90° woven E-glass composite.

Figure 11: Original grayscale OCT image of the epoxy/ unidirectional E-glass composite. (A.), Binary OCT image after automated image processing (B.).

Figure 12: OCT image of impact damaged epoxy/unidirectional E-glass composite. 0 μm from surface along the x-z plane (A.). Along the y-z plane showing placement of tows via polyester stitching (B.).

Figure 13: OCT image of impact damaged epoxy/unidirectional E-glass composite. 337 μm from surface along the x-z plane (A.). Along the y-z plane showing placement of tows via polyester stitching (B.).

Figure 14: OCT image of impact damaged epoxy/unidirectional E-glass composite. 460 μm from surface along the x-z plane (A.). Along the y-z plane showing placement of tows via polyester stitching (B.).

Figure 15: OCT image of impact damaged epoxy/unidirectional E-glass composite. 550 μm from surface along the x-z plane (A.). Along the y-z plane showing placement of tows via polyester stitching (B.).

Figure 16: OCT image of impact damaged epoxy/unidirectional E-glass composite. 652 μm from surface along the x-z plane (A.). Along the y-z plane showing placement of tows via polyester stitching (B.).

TABLE CAPTIONS

Table 1: Values of experimental and calculated permeabilities and corresponding Brinkman fraction.

REFERENCES

- ¹ Identification of a commercial product is made only to facilitate experimental reproducibility and to adequately describe experimental procedure. In no case does it imply endorsement by NIST or imply that it is necessarily the best product for the experimental procedure.
- ² D. Bodamer, *Civil Engineering*, **68(1)**, 56(1998).
- ³ F. Billmeyer, Jr. "Textbook of Polymer Science", 3rd ed.; Wiley & Sons: New York, 1984.
- ⁴ E. Pleudemann, "Silane Coupling Agents", 2nd ed.; Plenum Press: New York, 1991.
- ⁵ M. Naitove and J. Gaspari, *Plastics Technology*, **43(3)**, 32(1997).
- ⁶ Anonymous, *Manufacturing Engineering*, 12(1995).
- ⁷ Anonymous, *Manufacturing Engineering*, **120(3)**, 48(1998).
- ⁸ S. Mraz and M. Dibble, *Machine Design*, **65(18)**, 166(1993).
- ⁹ K. Jost, *Automotive Engineering*, 104, 27(1996).
- ¹⁰ S. Silverman, *Hart's Petroleum Engineer International*, **71(12)**, 21(1998).
- ¹¹ L. Cercone and J. Korff, *Civil Engineering*, 67(7), 60(1997).
- ¹² H. Thippeswamy, J. Franco, and H. GangaRao, *Concrete International: Design and Construction*, **20(6)**, 47(1998).
- ¹³ M. Larson, *Quality*, **37(9)**, 30(1998).
- ¹⁴ N. Patel and J. Lee, *Polymer Composites*, **16(5)**, 386(1995).
- ¹⁵ N. Patel, V. Rohatgi, and J. Lee, *Proc. 49th Ann. SPI Compos. Inst. Conf.*, Session 10-D (1994).
- ¹⁶ N. Patel, V. Rohatgi, and J. Lee, *Polymer Composites*, **14**, 161(1993).
- ¹⁷ S. Ghlorse, *SAMPE Quarterly*, **24**, 54(1993).
- ¹⁸ J. Thomason and A. Knoester, *Journal of Materials Science Letters*, **9**, 258(1990).
- ¹⁹ J. Izatt, M. Hee, G. Owen, E. Swanson, and J. Fujimoto, *Optics Letters*, **19(8)**, 590(1994).
- ²⁰ S. Wooh and I. Daniel, *Materials Evaluation*, **48(5)**, 1199(1994).
- ²¹ R. J. Dewhurst, R. He, and Q. Shan, "Defect visualization in carbon fiber composite using laser ultrasound," *Materials Evaluation*, **51(8)**, pp. 935-940, 1993.
- ²² A. Highsmith, and S. Keshav, *J. Comp. Tech. & Res.*, **19(1)**, 10(1997).
- ²³ M. Kortschot and C. Zhang, *Comp. Sci. & Tech.*, **53(2)**, 175(1995).
- ²⁴ R. Bossi and G. Georgeson, *Materials Evaluation*, **53(10)**, 1198(1995).
- ²⁵ K.-P. Hoh, H. Ishida, and J. Koenig, *Polymer Composites*, **11(3)**, 192(1990).
- ²⁶ B. Blumich, *Adv. Mater.*, **3(5)**, 237(1991).
- ²⁷ P. Jezzard, C. Wiggins, T. Carpenter, L. Hall, J. Barnes, P. Jackson, and N. Clayden, *J. Mat Sci.*, **27(23)**, 6365(1992).

-
- ²⁸ J. Dunkers, C. Zimba, K. Flynn, D. Hunston, R. Prasankumar, X. Li and J. Fujimoto, *Proceedings of SPIE's International Symposium on Nondestructive Evaluation Techniques for Aging Infrastructure and Manufacturing*, March 3-5, 1999.
- ²⁹ J. P. Dunkers, R. S. Parnas, C. G. Zimba, R. S. Peterson, K. M. Flynn, J. G. Fujimoto, and B. E. Bouma, *Composites, Part A*, **30(2)**, 139(1999).
- ³⁰ S. Ranganathan, G. Wise, F. Phelan Jr., R. Parnas, S. and Advani, *Advanced Composites X: Proceedings of the 10th Annual ASM/ESD Advanced Composites Conference and Exposition (ACCE94)*, ASM International, 309(1994).
- ³¹ T. S. Lundström, Ph.D. Thesis, Luleå University of Technology, Luleå, Sweden, 1996.
- ³² F. R. Phelan, Y. Leung, and R. S. Parnas, *Journal of Thermoplastic Composite Materials*, **7**, 208(1994).
- ³³ S. Ranganathan, G. Wise, F. Phelan Jr., R. Parnas, and S. Advani, *Advanced Composites X: Proceedings of the 10th Annual ASM/ESD Advanced Composites Conference and Exposition (ACCE94)*, ASM International, 309(1994).
- ³⁴ J. Dunkers, C. Zimba, D. Hunston, K. Flynn, R. Parnas, J. Fujimoto, and J. Herrmann, Proc. the ASC 13th Tech. Conf. Comp. Mat., 1626(1998).
- ³⁵ D. J. Bradley, D. O. Adams, and H. E. Gascoigne, *J. of Rein. Plas & Comp.*, **17(11)**, 989(1998).
- ³⁶ R. S. Parnas, Chapter 8. Preform Permeability, in *RTM for Aerospace Applications*, T. K. Kruckenberg (ed.), Chapman & Hall, 1999.
- ³⁷ J. Dunkers, F. Phelan, C. Zimba, K. Flynn, R. Peterson, R. Prasankumar and J. Fujimoto, *Proc. 57th Ann. ANTEC Conf.*, May 2-6, 1999, New York, NY.
- ³⁸ R. Parnas, and A. Salem, *Polymer Composites*, **14(5)**, 383(1993).
- ³⁹ H. Friedman, R. Johnson, B. Miller, D. Salem, R. and Parnas, *Polymer Composites*, **18(5)**, 663(1997).
- ⁴⁰ F. Phelan Jr. and G. Wise, *Composites: Part A*, **27A(1)**, 25(1996).
- ⁴¹ M. Spaid and F. Phelan Jr., *Phys. Fluids*, **9(9)**, 2468(1997).
- ⁴² M. Spaid and F. Phelan Jr., *Composites: Part A*, **29**, 749(1998).
- ⁴³ S. Ranganathan, R. Easterling, S. Advani, and F. Phelan Jr., *Polymers & Polymer Composites*, **6(2)**, 63, (1998).
- ⁴⁴ R. Parnas, K. Flynn, and M. Dal-Favero, *Polymer Composites*, **18(5)**, 623(1997).
- ⁴⁵ E. D. Blodget, J. G. Miller, and S. M. Freeman, *Review of Progress in Quantitative Nondestructive Evaluation*, D. O. Thompson and S. E. Chimenti, eds, 1227, Plenum, New York, 1986.

FIGURES

Figure 1

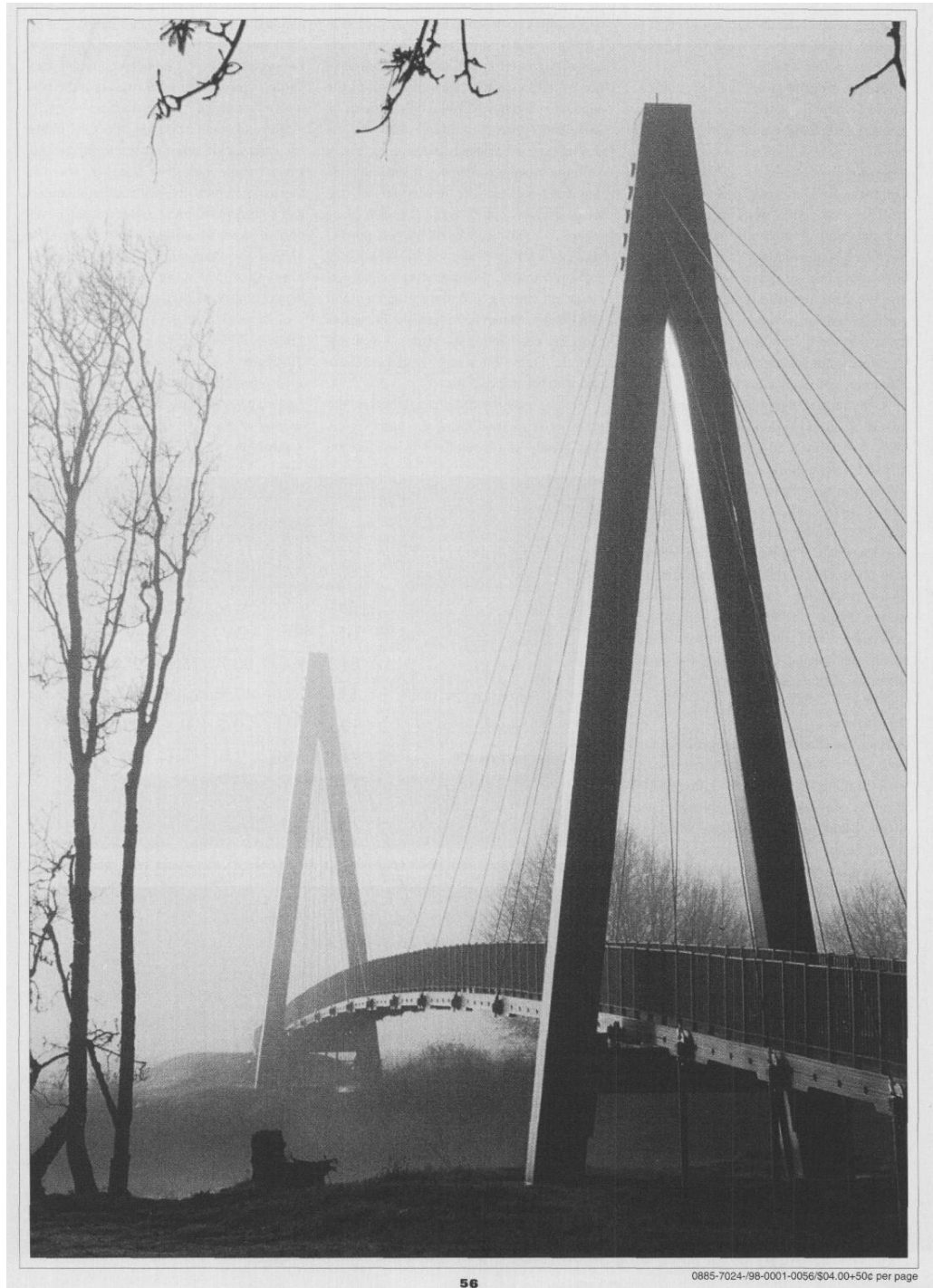


Figure 2

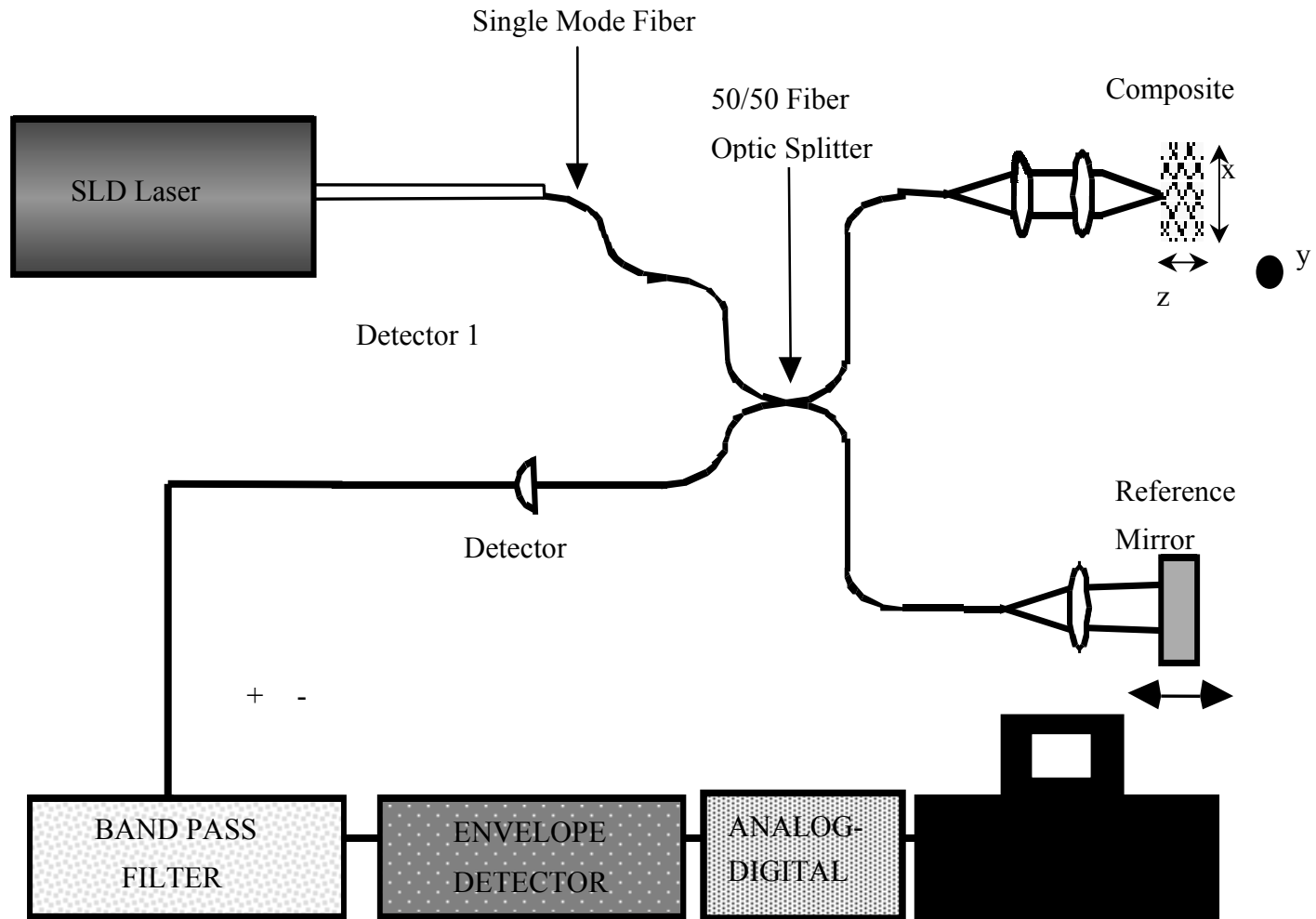


Figure 3

Orientation of Composite with Laser Beam

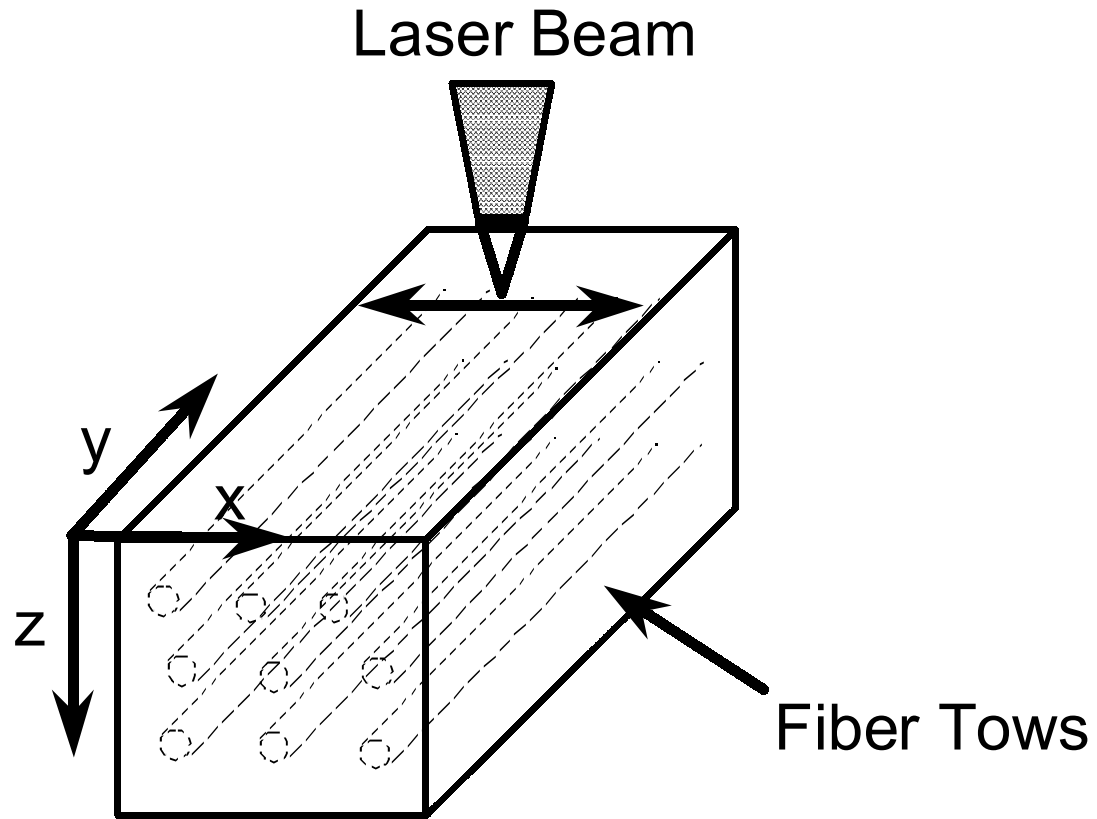


Figure 4

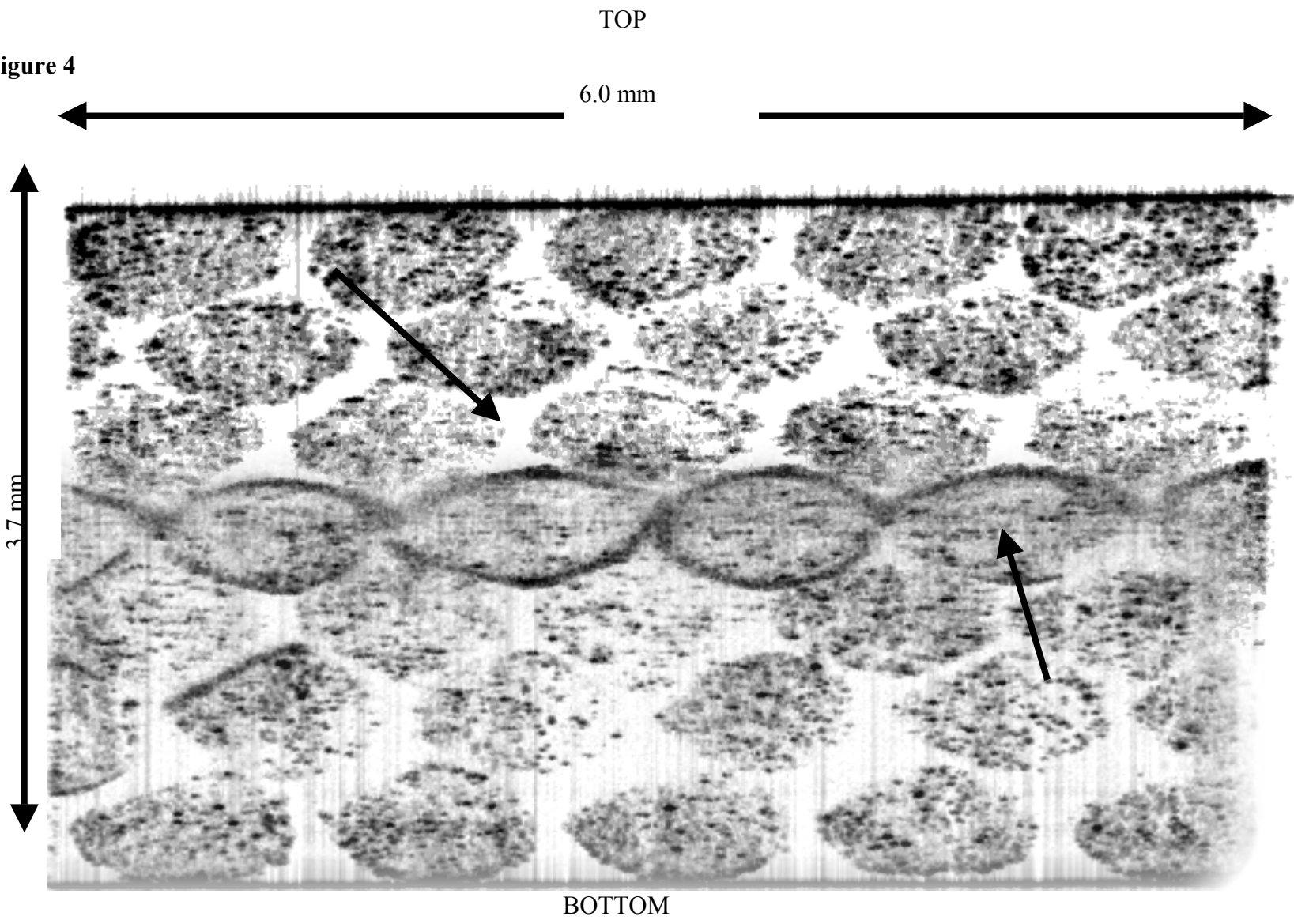


Figure 5

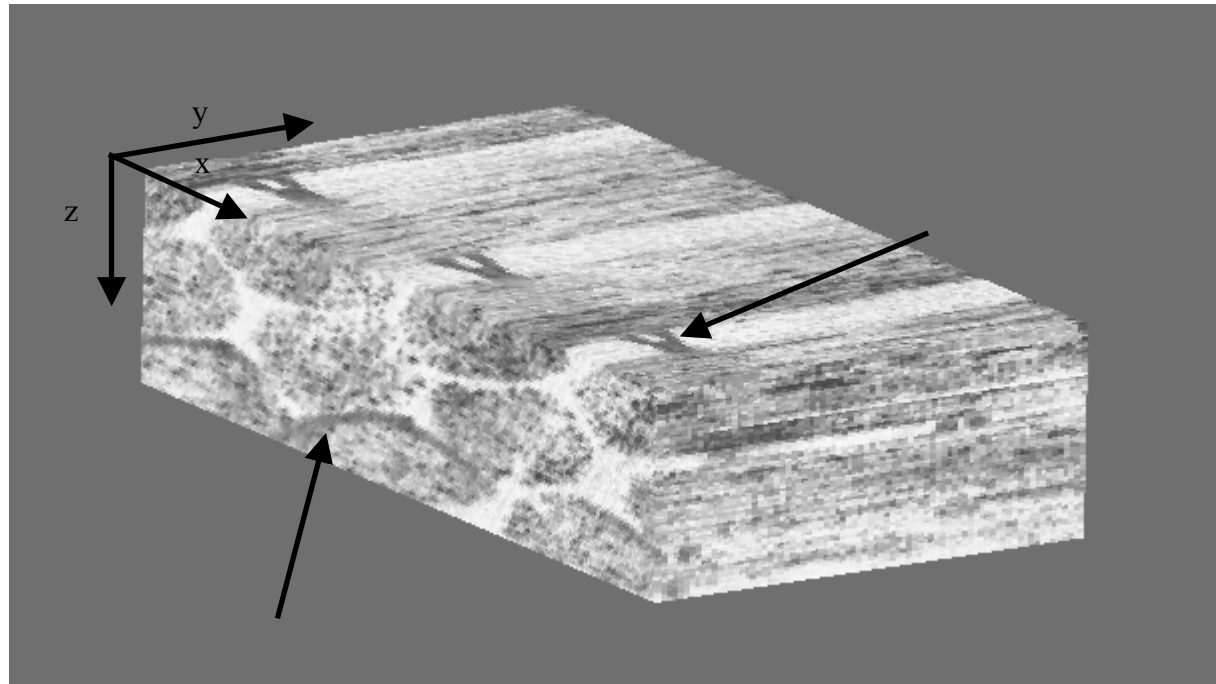


Figure 6

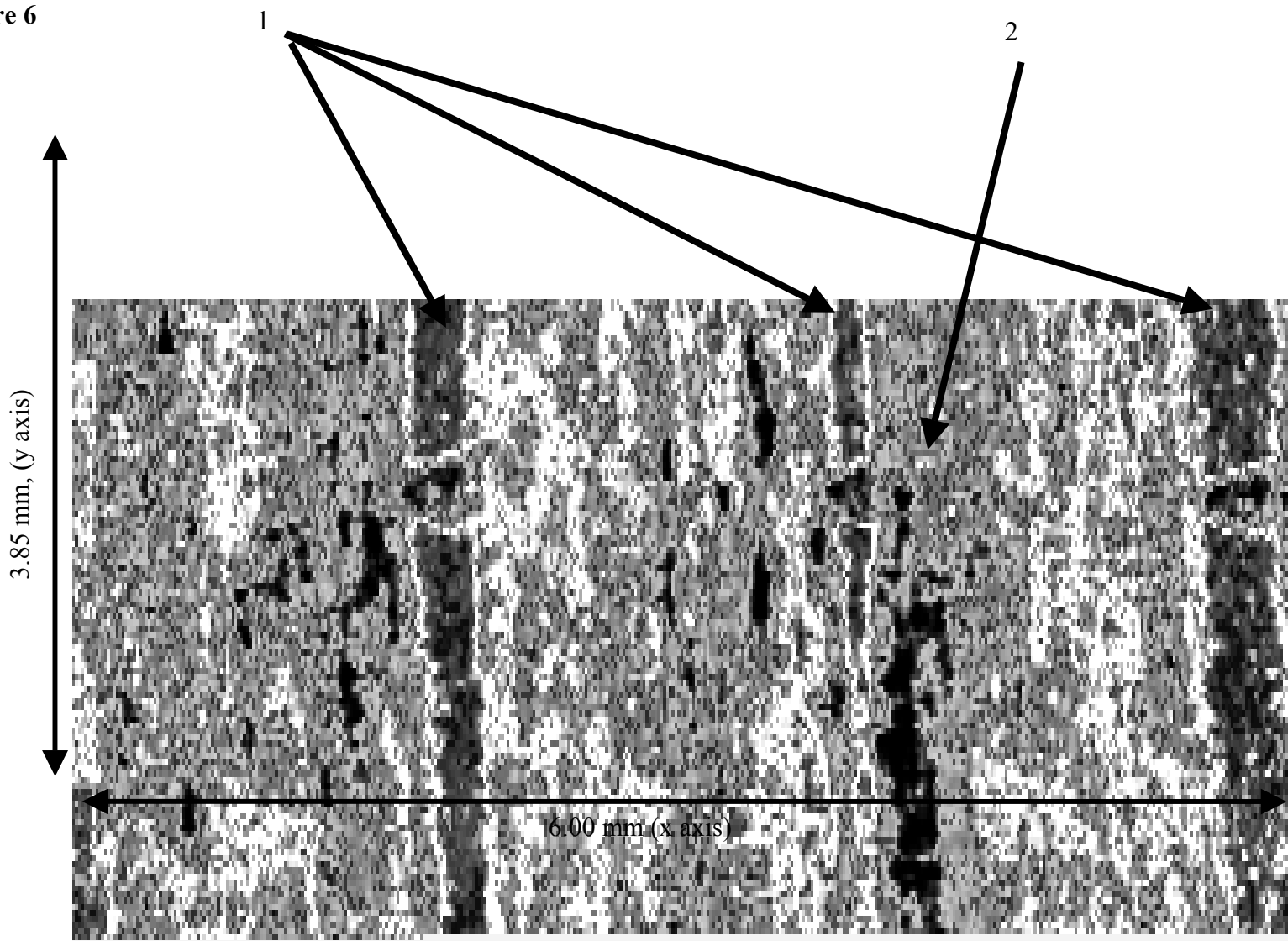


Figure 7

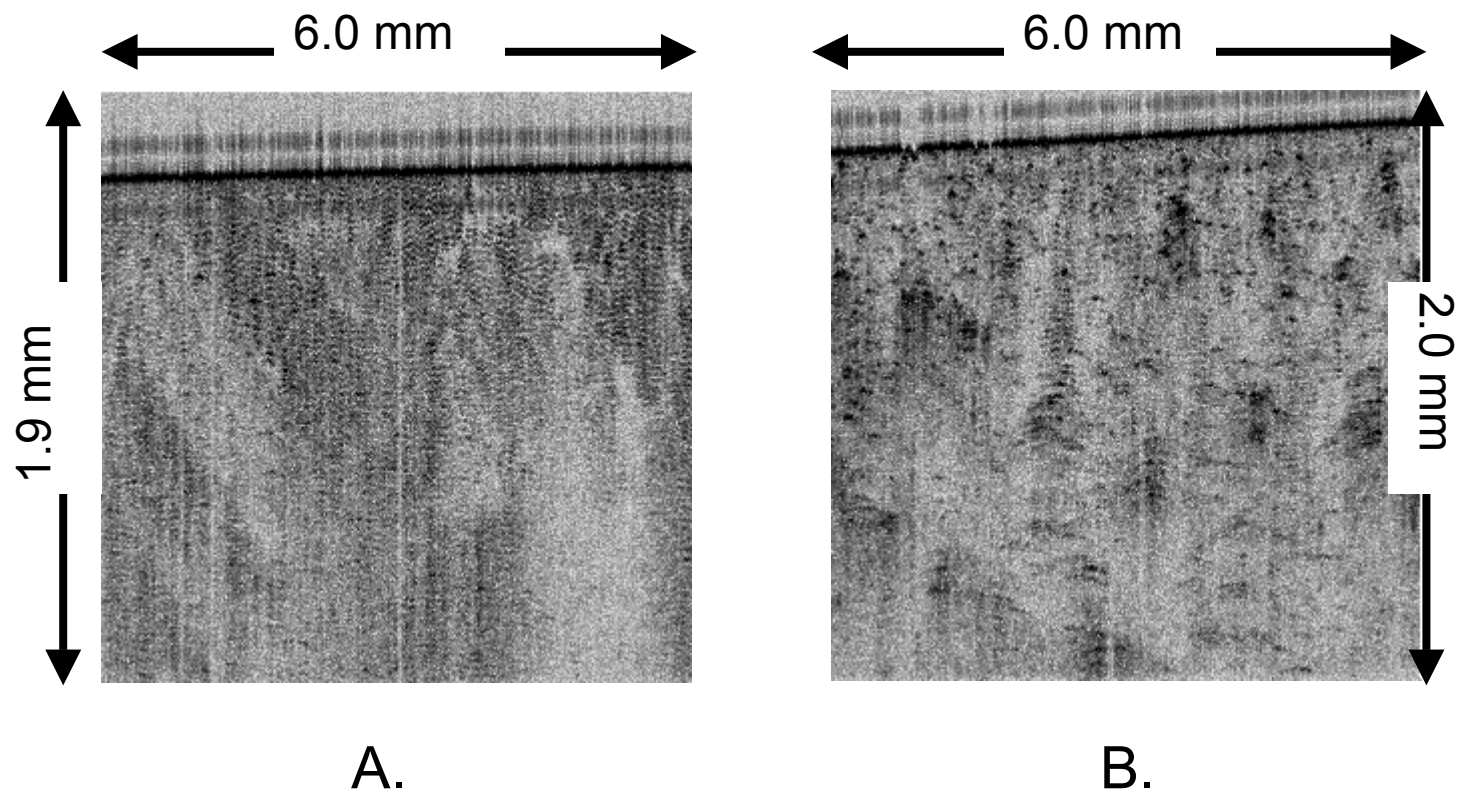


Figure 7

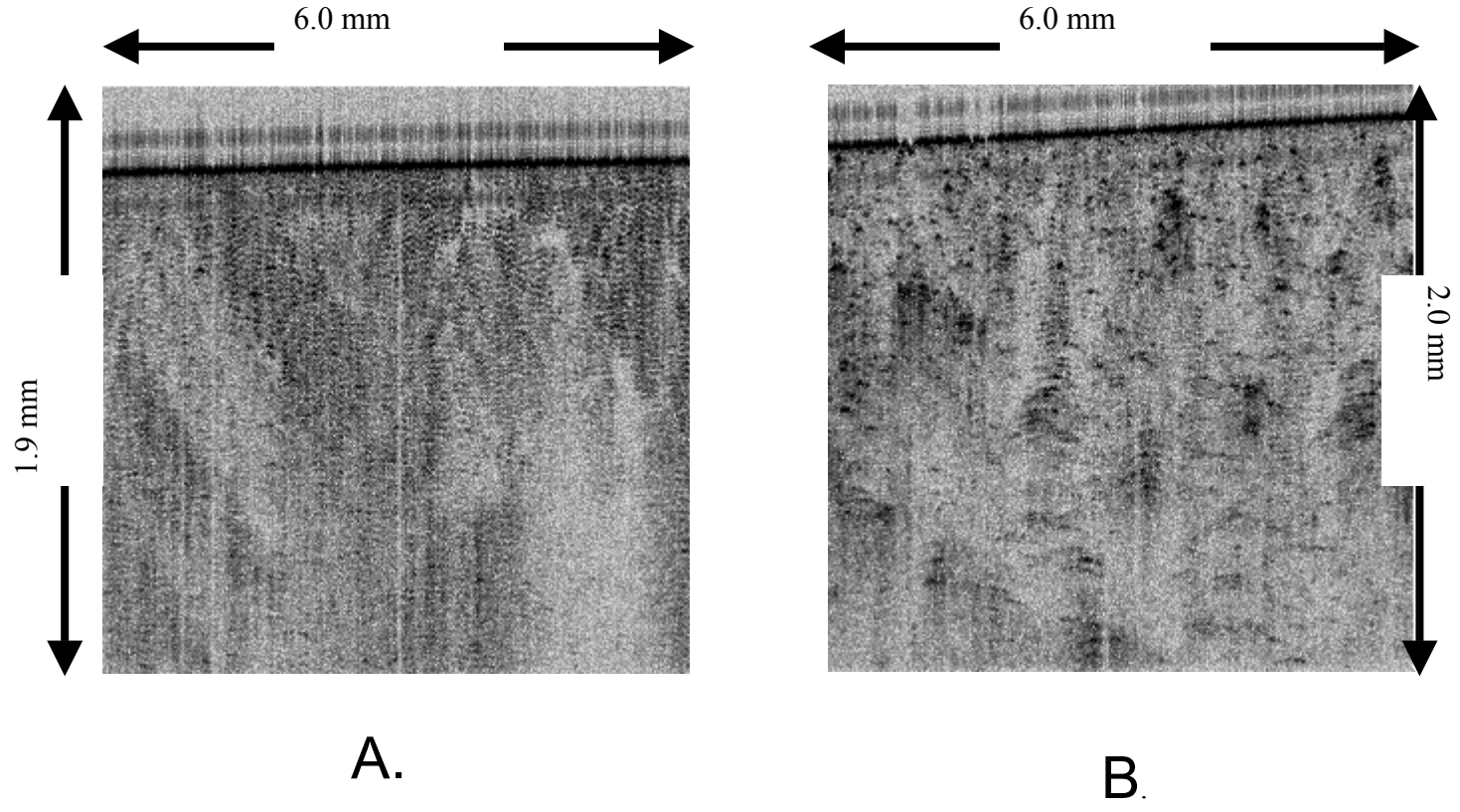


Figure 8

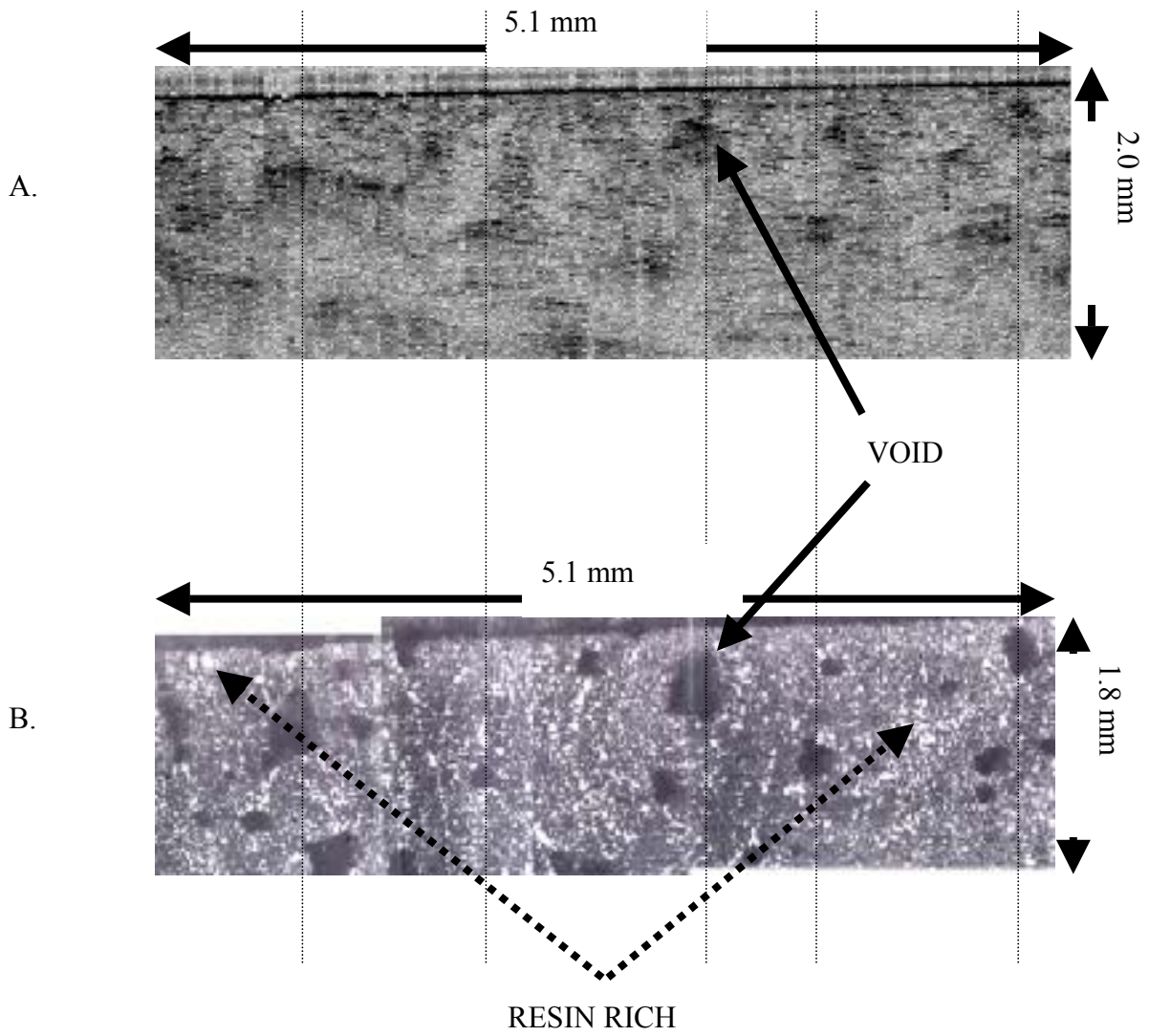


Figure 9

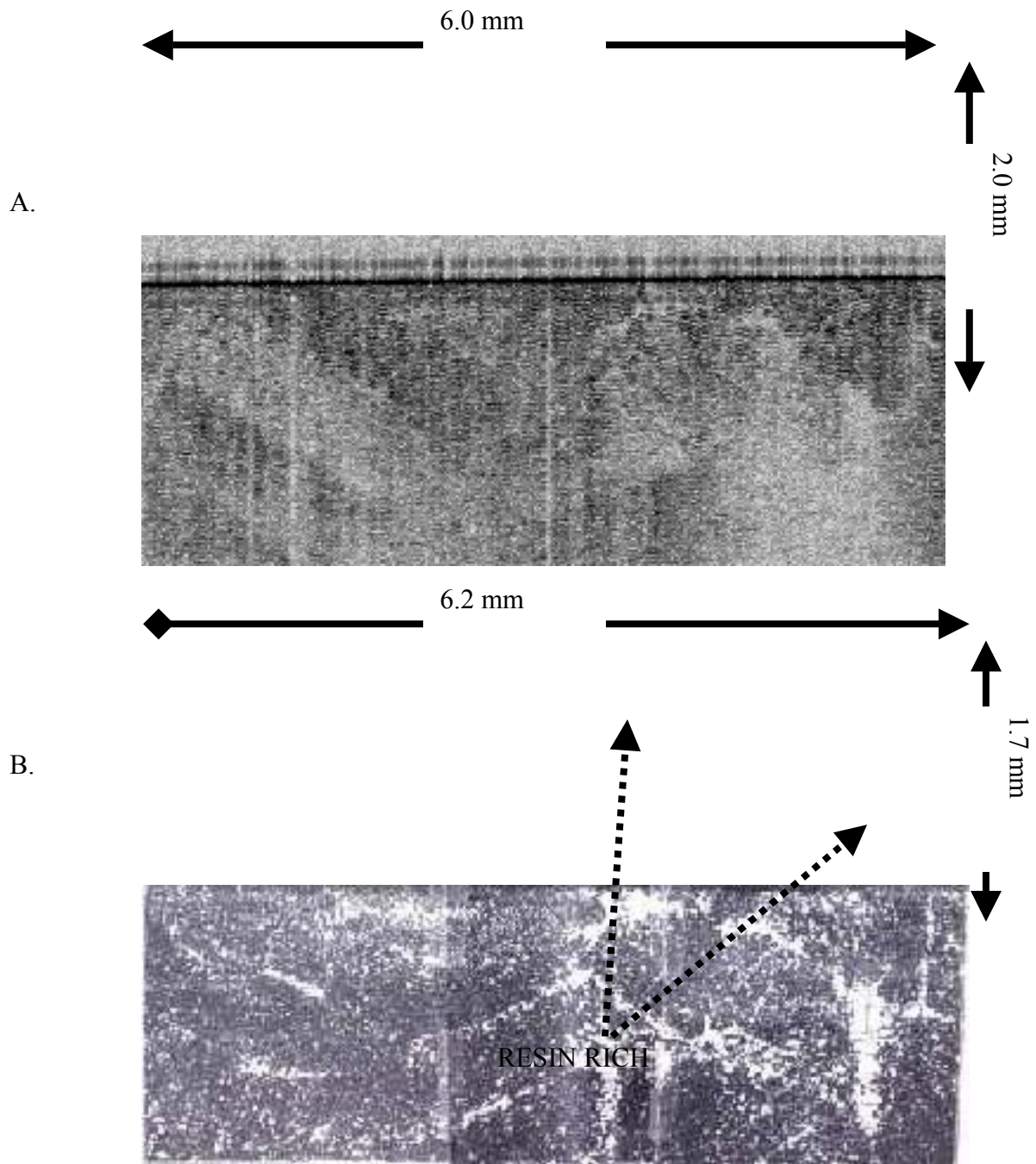


Figure 10

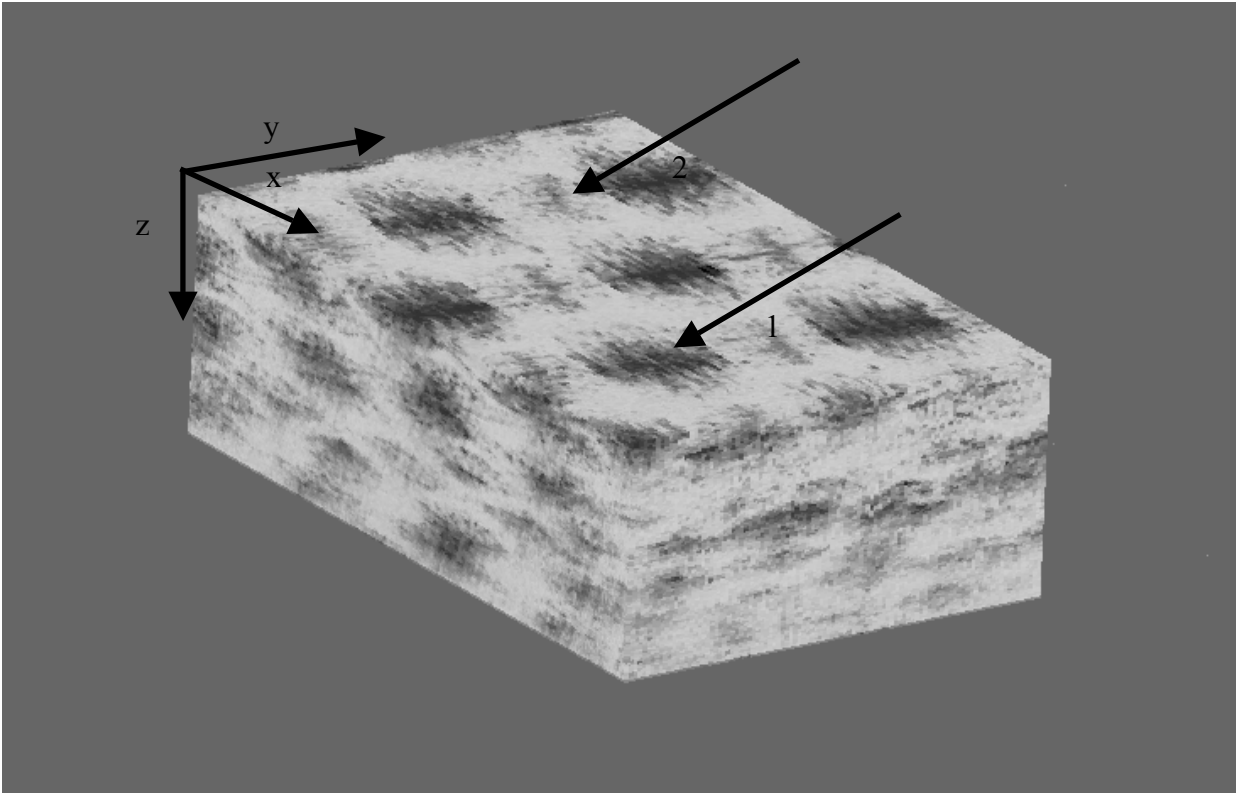


Figure 11

A.



B.



Figure 12

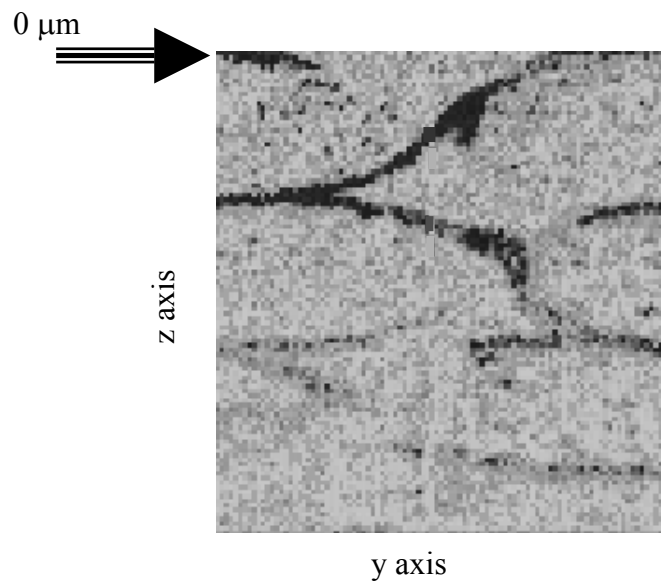
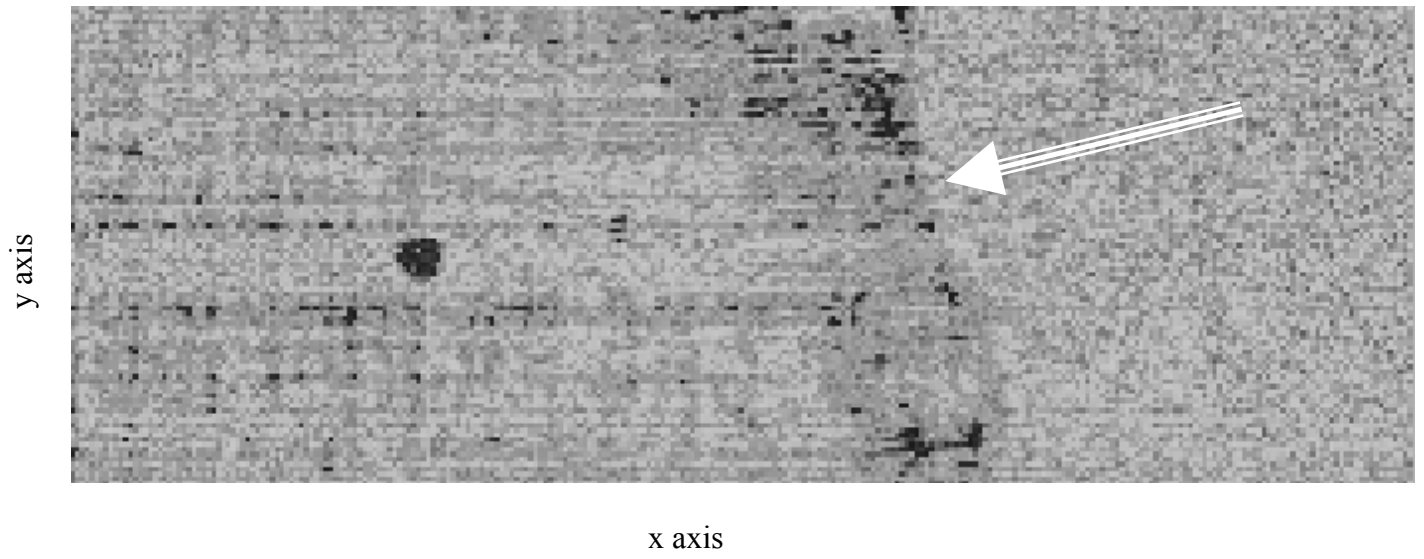


Figure 13

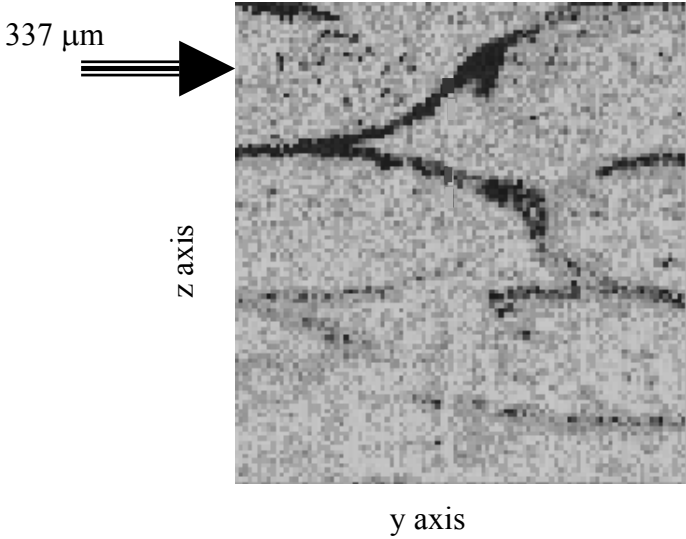
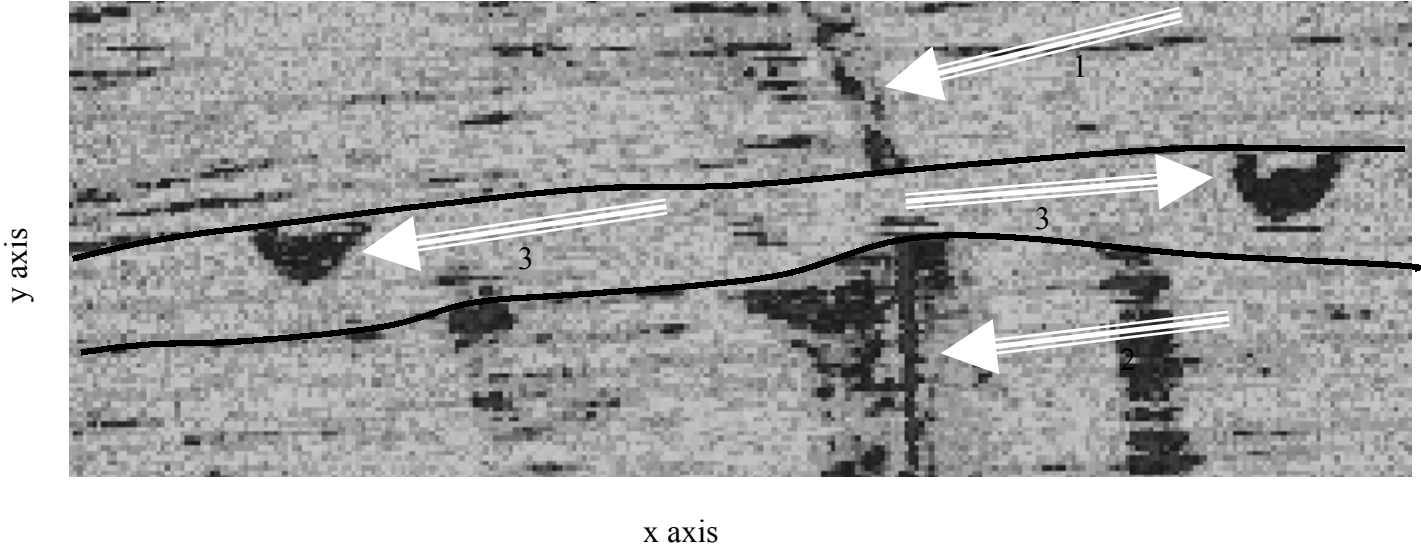


Figure 14

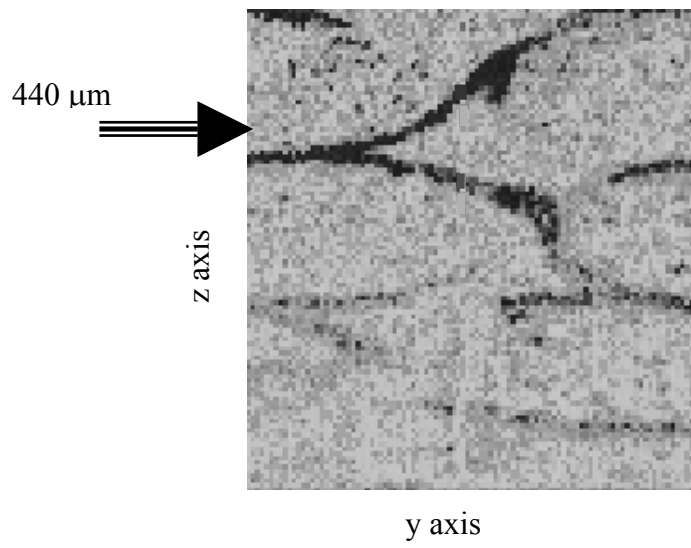
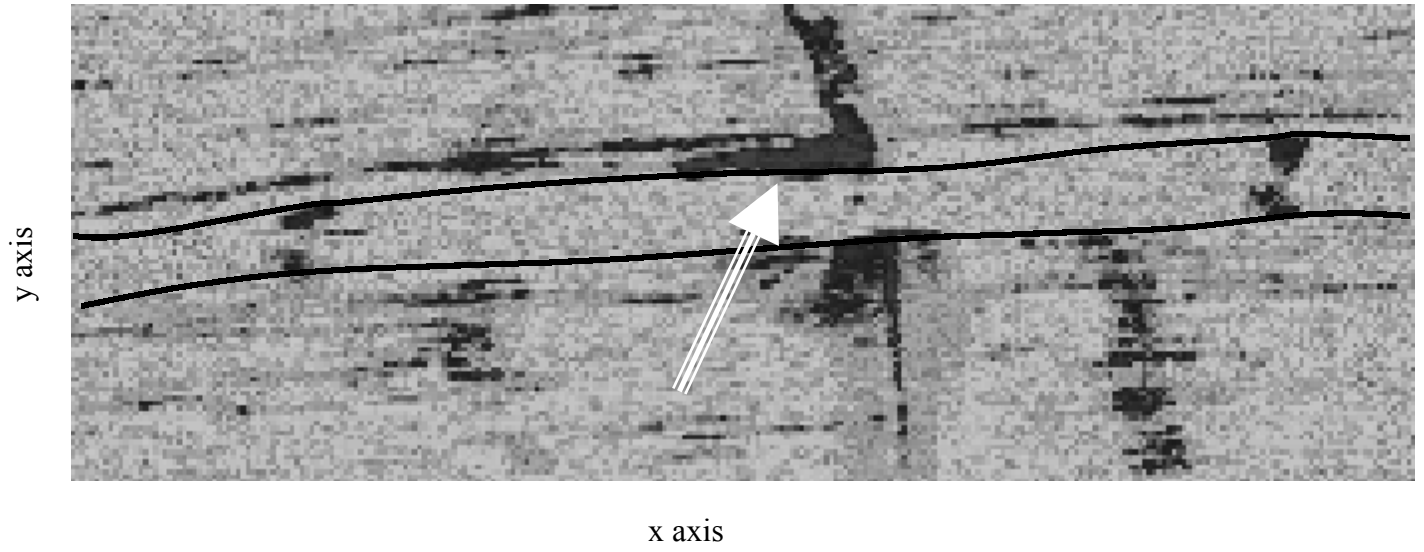


Figure 15

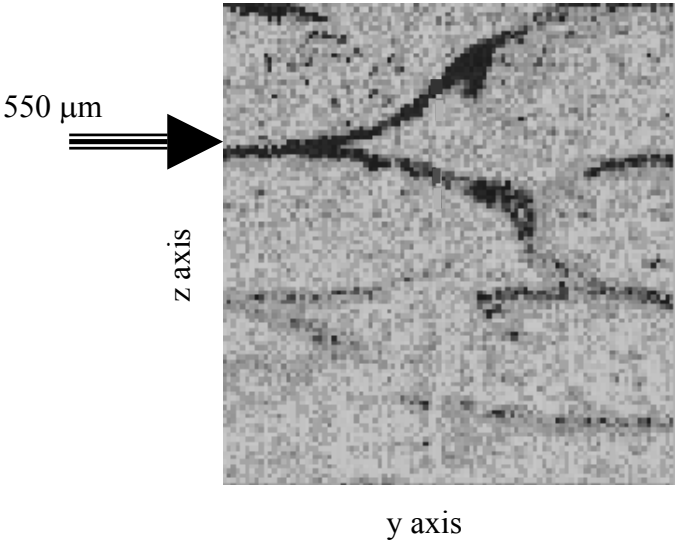
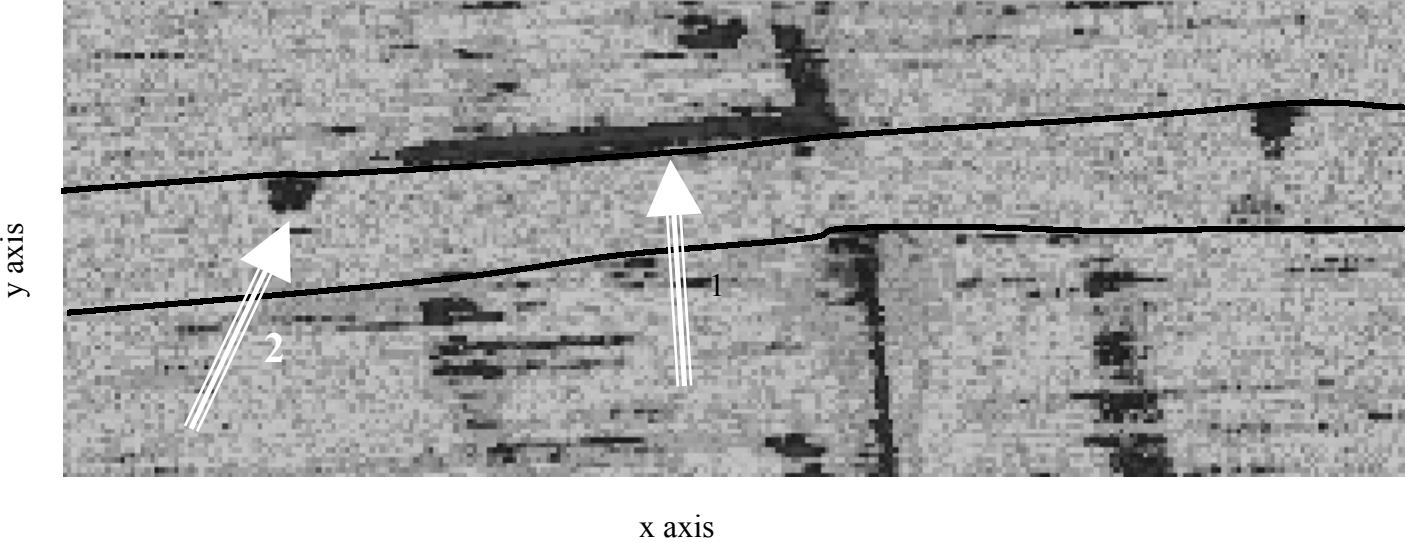


Figure 16

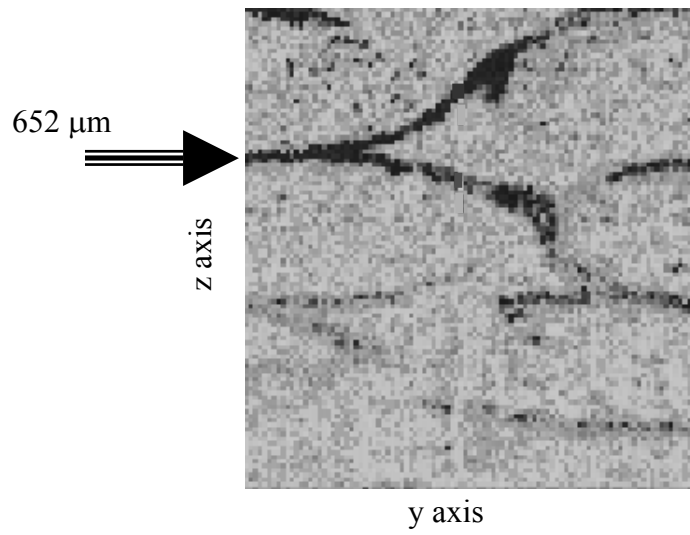
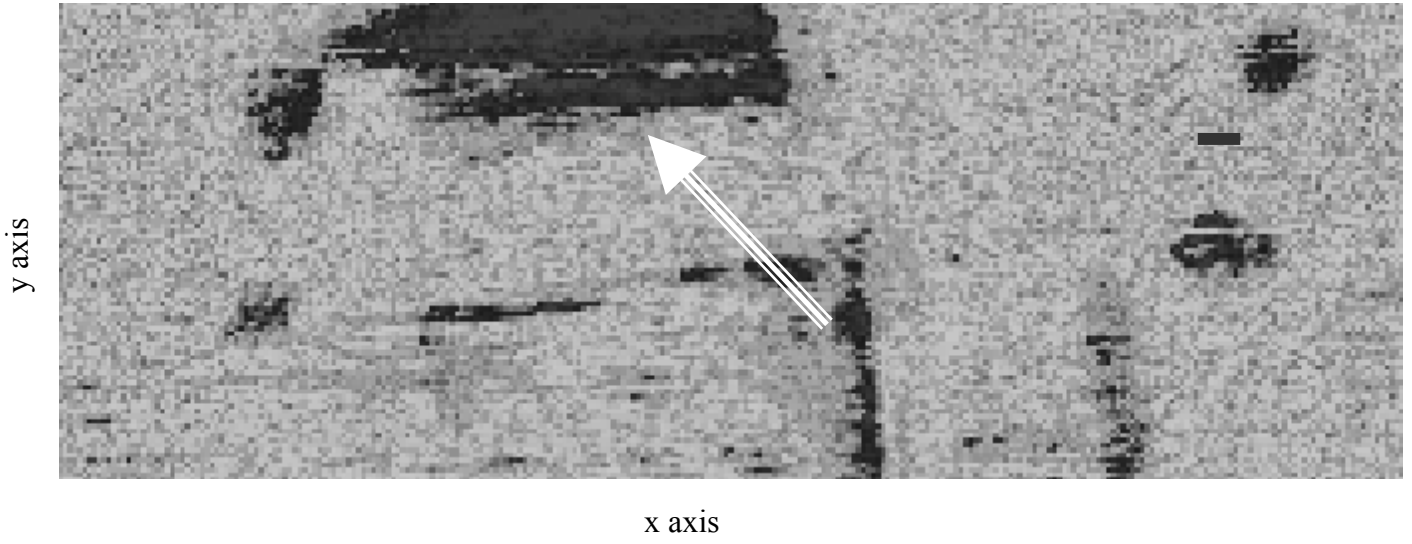


Table 1

Sample Name	Type of Processing	Image Set	Axial K $\times 10^{-4}$ (mm ²)	Transverse K $\times 10^{-4}$ (mm ²)	Anisotropy Ratio	Brinkman Fraction
Experimental	-	-	5.3 \pm 1.1	-	-	0.770
Data 1	Manual	87-91	4.45	0.882	5.06	0.767
Data 2	Manual	75-95	3.81	0.992	4.11	0.788 \pm 0.021
Data 3	Automated No Smoothing	75-95	2.83	0.654	4.32	0.768 \pm 0.021
Data 4	Automated Smoothing	75-95	3.18	0.991	3.21	0.750 \pm 0.027
Data 5	Automated Smoothing	4-24	5.09	0.934	5.45	0.727 \pm 0.014
Data 6	Manual Roughened	75-95	2.73	0.662	4.12	0.795 \pm 0.021
Data 7	Manual Dilated	75-95	2.99	0.767	3.90	0.837 \pm 0.020